Effect of Porosity on Deformation, Damage, and Fracture of Cast Steel

R.A. HARDIN and C. BECKERMANN

A combined experimental and computational study is performed to investigate the effect of centerline shrinkage porosity on deformation, damage, and fracture of cast steel under tensile testing. Steel plates containing shrinkage porosity are cast in sand molds, machined into test coupons, and tensile tested to fracture. The average volumetric porosity in the gage section of the specimens with porosity ranges from 0.10 to 0.27 pct. Ductility in the test castings with porosity is markedly reduced with the percent elongation data ranging from 12.8 to 19.6 pct; *vs* 22 pct elongation for the sound material. Radiographic imaging is used to measure and reconstruct the porosity field in the test specimens. The reconstructed porosity field is then used in a finite-element stress analysis simulating the tensile testing. Local elastic properties are reduced according to the porosity fraction present. Porous metal plasticity theory is used to model the damage due to porosity and the fracture. Good agreement is obtained between the measured and predicted stress–strain curves and fracture behaviors. The reduction in ductility is predicted well by comparing the measured and the simulated elongations. The computational modeling approach used in this study allows for a detailed evaluation of the effect of porosity, including its size, shape, and location, on the fracture behavior of steel castings.

DOI: 10.1007/s11661-013-1669-z
© The Minerals, Metals & Materials Society and ASM International 2013

I. INTRODUCTION

STEEL castings are under-utilized because of uncertainties in their performance and lack of expertise in casting design. Discontinuities in castings, like porosity, play an important role in casting underutilization. Porosity creates uncertainty in a design's robustness, since there are no methodologies for including its presence in the design. As a result, designers employ overly large safety factors to ensure reliability leading to heavier components than necessary. Contributing to the issue, the processes of designing and producing castings are usually uncoupled except for the specification of nondestructive evaluation (NDE) requirements. Unless design engineers have test data or experience for a part, they call for NDE requirements without knowing how this relates to part performance. By predicting porosity accurately from casting simulation and realistically modeling its effects on the part performance, engineers can develop robust designs that are tolerant of the porosity and reliable. In the current study, engineering approaches have been applied to simulate the effect of porosity on deformation, damage, and fracture for a cast steel during tensile testing, and the simulation results are compared with measurements.

R.A. HARDIN, Research Engineer, and C. BECKERMANN, Professor, are with the Department of Mechanical and Industrial Engineering, University of Iowa, Iowa City, IA 52242. Contact e-mail: becker@engineering.uiowa.edu

Manuscript submitted August 31, 2012.
Article published online February 28, 2013

The material used in this study is ASTM A216 Grade WCB steel. It is a cast carbon steel having a combination of good ductility and strength. It has the following chemical composition (maximum wt pct): C 0.3; Mn 1.0; P 0.035; S 0.035; Si 0.6; Cu 0.3; Ni 0.5; Cr 0.5; Mo 0.2; and V 0.03; and the total of Cu, Ni, Cr, Mo, and V cannot exceed 1.0 wt pct. At room temperature, Grade WCB steel has a yield strength and a tensile strength of 248 and 485 MPa, respectively, and 22 pct elongation as minimum tensile requirements in ASTM A216. Failure of such ductile metals occurs on the microscopic scale by mechanisms of void nucleation, growth, and coalescence.[1] Voids can pre-exist as microporosity and can also nucleate from imperfections like second-phase particles. After nucleation, voids grow with increasing hydrostatic stress and local plastic straining. As voids nucleate and grow, the void (or porosity) volume fraction increases. The voids begin to interact, and the porosity fraction at which interactions between voids begins is the critical porosity volume fraction f_c. As plastic strain continues to increase, local necking and coalescence occur in the material between voids until a connected chain of voids forms and failure occurs. The porosity fraction at which fracture occurs is the failure porosity volume fraction f_F.

The effects of porosity on the structural performance of carbon and low alloy steel castings on the macroscopic scale are not as clearly defined as they are on the microscopic scale. In previous studies, the effects of large amounts of porosity on stiffness and fatigue life were investigated.[2,3] Porosity less than a few percent does not result in a measurable loss of stiffness, or large stress concentrations, or stress redistribution, but it

greatly affects fatigue resistance.[4,5] Also, the presence of low-level porosity will reduce the ductility of metals since microvoids pre-exist before any stress is applied and the nucleation stage is bypassed. Porosity larger than a few percent in metals causes gross section loss, and locally reduces their effective stiffness.[6–8] This higher-level porosity is not uniformly distributed throughout the entire cast part, and the material properties in the casting are heterogeneous. As a result, stress redistribution occurs in parts because of macropores, and stress concentrations occur near them, which lead to localized plastic deformation and the development of microcracks causing failure. Generally speaking, the performance of a casting with macroporosity depends on the amount, size, and location of porosity relative to the cast component's geometry and loading. All these factors must be considered together. Determining the effects of large levels of porosity on part performance is typically more case-by-case dependent than for lower levels.

It has been proposed that the stiffness and strength behaviors of porous materials can be categorized into three groups based on porosity amounts[9]: less than 10, 10 through 70 pct, and materials with greater than 70 pct. This division is promoted because the materials at the extremes (<10, and >70 pct) behave quite differently. The highest porosity group is not applicable to cast steels; these are foams and cellular structures. The elastic–plastic behavior of porous materials in the 10 through 70 pct porosity range exhibit a nonlinear dependence on the amount of porosity[2,6–9] The behavior of materials in the lowest range demonstrate a more linear dependence on porosity amount, assuming that voids do not interact[10] and by considering isolated pores,[11] or a uniform distribution of pores.[12] Applying the ductile failure micromechanical mechanisms described previously, one such micromechanics-based model is the porous metal plasticity model. It is available in the finite element analysis (FEA) software *ABAQUS*.[11–15] In the model, the volume fraction of porosity is a primary state variable, and the inelastic flow of the material is modeled as voids grow and coalesce at higher strains until failure occurs. Porous metal plasticity was developed assuming voids are spherical and grow as spheres. It also assumes the material's plastic behavior is dependent on hydrostatic pressure because of the porosity, and therefore neglects effects of shear stresses on porous material behavior. Considering this and the limitations of porous metal plasticity, there have been numerous developments in modeling of ductile fracture[16] addressing other void geometries and stress states. While not state-of-the-art, porous metal plasticity is a constitutive model readily available to designers of cast components, and can be a useful tool to investigate the effect of porosity on a casting's fracture behavior. It is a common constitutive model found in many commercial finite element packages. This article uses the porous metal plasticity model in FEA to predict the ductile fracture of cast steel with centerline porosity. The primary goal of the current study tests whether or not this commonly available model can predict the fracture of steel with relatively large amounts of porosity detectable through typical industrial radiography.

Here, castings with porosity were produced, made into plate specimens, and radiographed. The porosity was quantitatively determined from the radiographs. The castings underwent tensile testing. Using porosity data from the radiographs, finite element stress models of the test specimens with porosity were created, and the tensile testing simulated using an elastic–plastic material model. Results of the simulated fracture are compared here with the measured fracture to test the model's capabilities in predicting the fracture behavior of steel with centerline shrinkage porosity.

II. MATERIAL PREPARATION, MEASUREMENT, AND ANALYSIS

A. *Cast Specimens and Mechanical Testing*

For the tensile fracture study presented in this article, WCB steel specimens were produced from 2.5 cm thick × 12.7 cm wide vertically cast plates of two lengths (38.1 cm and 45.7 cm) as shown in Figure 1(a). The plates were designed through casting simulation with *MAGMAsoft*[17] to contain centerline shrinkage as shown in Figures 1(b) and (c). Five cast plates were produced and tested from the longer length castings, and four were produced and tested for the shorter-length castings. The letters "D" and "E" were used to identify the shorter and longer plates, respectively; followed by numbers 1 through 5. The cast plates were normalized and tempered, and machined into 19-mm-thick tensile test coupons with a gage section width of 86 mm as shown in the front and side views for the specimen in Figure 2(a). The tensile specimen dimensions for the plates with centerline porosity were determined from the ASTM E8 tensile test standard.[18] The positioning of the extensometer on the narrow/thickness face of the specimen is indicated in Figure 2(a). In Figure 2(b), a smaller tensile test specimen is shown, which was machined from the porosity-free (or "sound") section of a cast plate. The specimen shown in Figure 2(b) was tested to characterize the steel's fracture behavior in the absence of porosity. The sound steel specimen was taken from the top end of the plate, and its dimensions shown in front and end views in Figure 2(b) were taken from ASTM E8. Parameters in the porous metal plasticity model were determined by achieving good agreement between the measured and predicted sound steel tensile curves. Tensile testing of the sound material was performed at the University of Iowa, and the steel plates with porosity were tested at the SSAB Americas Montpelier, Iowa Steelworks. Examining the fracture surfaces of the plates with porosity, the porosity was found to lie about the mid-thickness of the plates as expected from centerline porosity.

B. *Radiographic Porosity Measurement, Testing, and Fracture Analysis of the Specimens*

Film radiography was performed on the as-cast plates at the foundry where they were produced. All plates

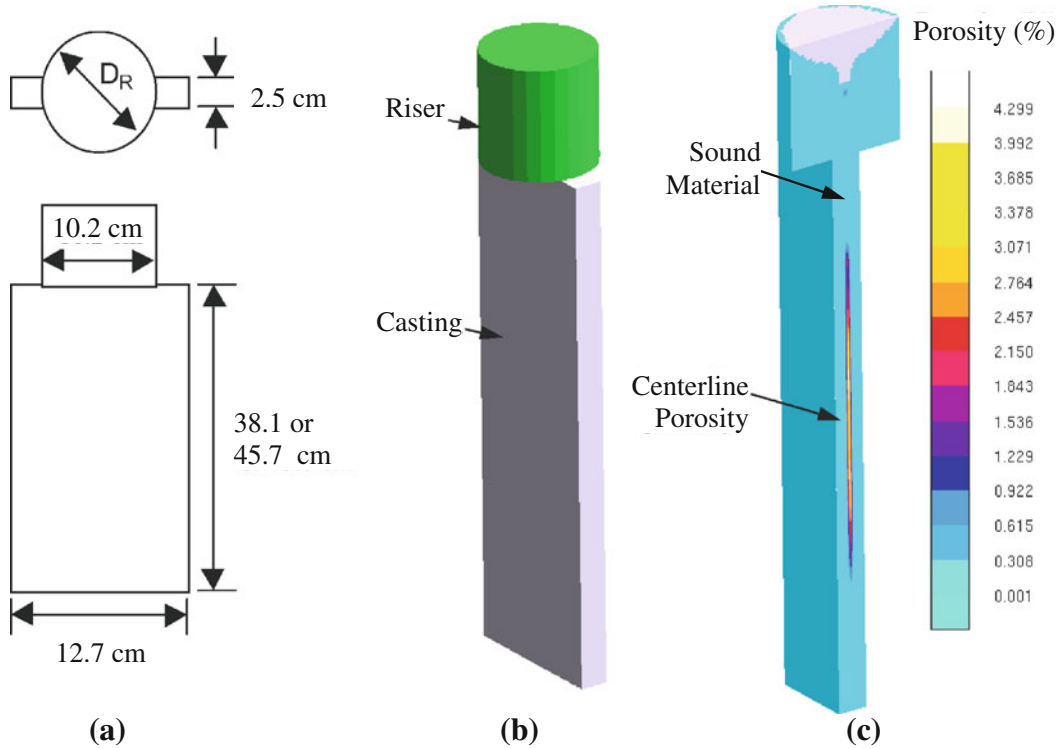

Fig. 1—(*a*) Top and front view diagrams of casting geometry (not to scale), (*b*) Casting simulation model for 45.7-cm-long plate, (*c*) centerline porosity prediction at mid-width using MAGMAsoft.[16]

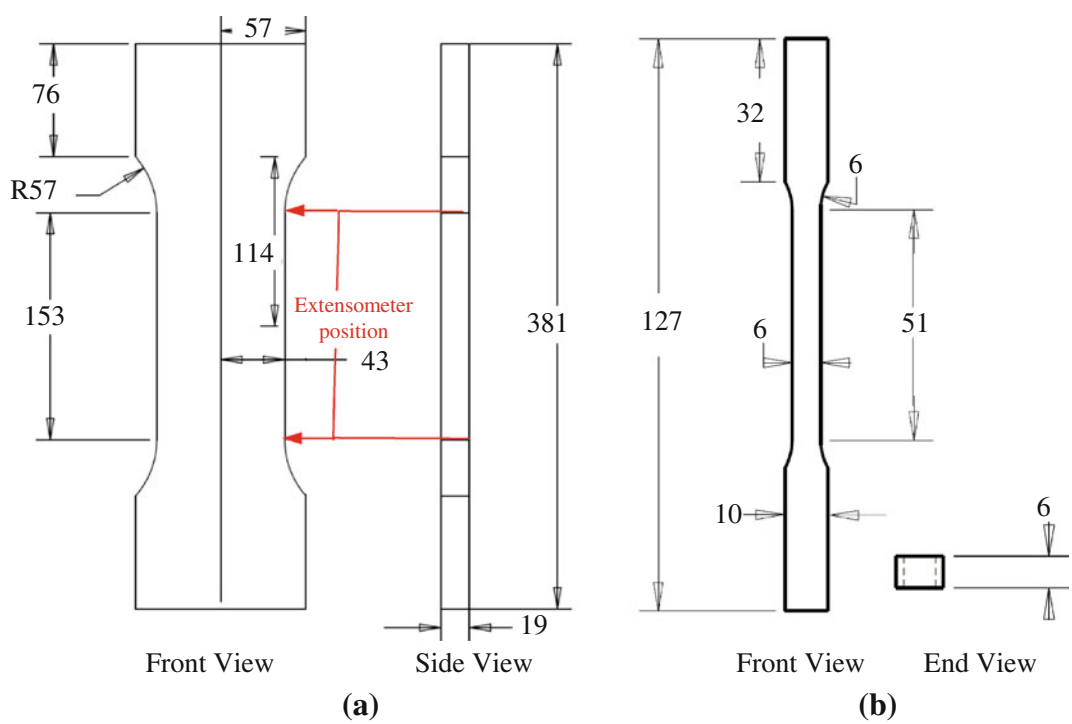

Fig. 2—Tensile testing specimens with dimensions in mm. (*a*) Front and side views of tensile test plate used for measurements with steel containing centerline shrinkage having a 19-mm-thick by 86-mm-wide gage section, and (*b*) front and end views of smaller test specimen used in tensile testing of the steel without porosity having a 6 mm square gage section.

were found to contain shrinkage porosity of levels 4 or 5 according to the radiographic testing standard ASTM E446.[19] In the standard, level 5 signifies the worst level of porosity defect, and level 1 signifies the least defective. Since the cast plates had porosity of levels 4 or 5, they would typically be scrapped at the foundry. After

machining and before testing, digital radiographs of the plate tensile test coupons with centerline shrinkage and the sound specimen were taken at 16-bit gray scale and 10 pixels per mm at Alloyweld Inspection Co. in Bensenville, Illinois. The radiograph of the sound specimen was free of any indications of shrinkage or other defects. Stepped gage blocks were placed in the radiographs of the plate specimens with centerline shrinkage as shown in Figure 3(a). Using the gage blocks and image analysis, a calibration curve of radiographic gray level *vs* plate thickness was determined for each radiograph. All curves were found to be within the same margin of error, but the individual radiograph calibration curves were used in analyzing the porosity level in the plates. Filtering and background corrections were performed, and only indications identified by image analysis were analyzed for porosity level as seen Figure 3(b). The thickness of the steel, as shown in Figure 3(c), was determined from the gray level *vs* thickness calibration curve. Finally, the measured porosity fraction through the plate thickness at each pixel of the radiograph was calculated by dividing the thickness of steel measured from the radiograph by the nominal machined plate thickness t_{plate} (19.1 mm) which is shown in Figure 3(d). Given the radiography equipment used, and the image analysis, the detectable threshold porosity fraction for the current study was estimated to be 1.5 pct. A radiograph for the specimen D3 is shown in Figure 4(a), where the fracture region is indicated by the area in the box. The fracture region on the radiograph was determined from the fractured specimen by measuring from the gripped plate ends and using punch marks made before testing on the narrow/edge faces of the specimens. A box is used to identify the fracture region due to the irregularity of the fracture surface and the uncertainty in the measurements. Since the tensile testing force was applied along in the length direction of the specimen, the cross section porosity normal to the force was determined as plotted in Figure 4(b) along the specimen length. Note here that positive distances are above the plate mid-length and negative values below. The overall average porosity in the gage section of each test plate was determined by averaging all the pixel measurements within the gage section, and as indicated in Figure 4(b) it is about 0.19 pct for specimen D3. The maximum cross section porosity for specimen D3 in Figure 4(b) is seen to be about 0.8 pct, and it falls within the observed fracture region along the length. For specimen D3, the fracture region is seen to correspond with a region of relatively high cross sectional porosity along the gage length, and this correspondence was observed in the other specimens as well. As shown in Figure 5, the average gage section porosity for all specimens was determined, ranging from 0.07 to 0.23 pct.

The tensile testing results for the sound WCB steel and the steel containing centerline porosity are shown in Figure 6. Note the sound material has the greatest elongation at fracture. The "D" centerline shrinkage porosity specimens (the shorter-length plates) generally have greater elongations than the "E" family of plates, but the most ductile of the plates with porosity was plate E1. In addition, the tensile curve for plate E1 appears quite different from the other curves and has much lower yield and ultimate strengths.

Unfortunately, X-ray tomography was not performed on the steel specimens because of their relatively large size. Because of this, an assumption about how the porosity measured from the radiographs was distributed through the plate thickness had to be made. Regions

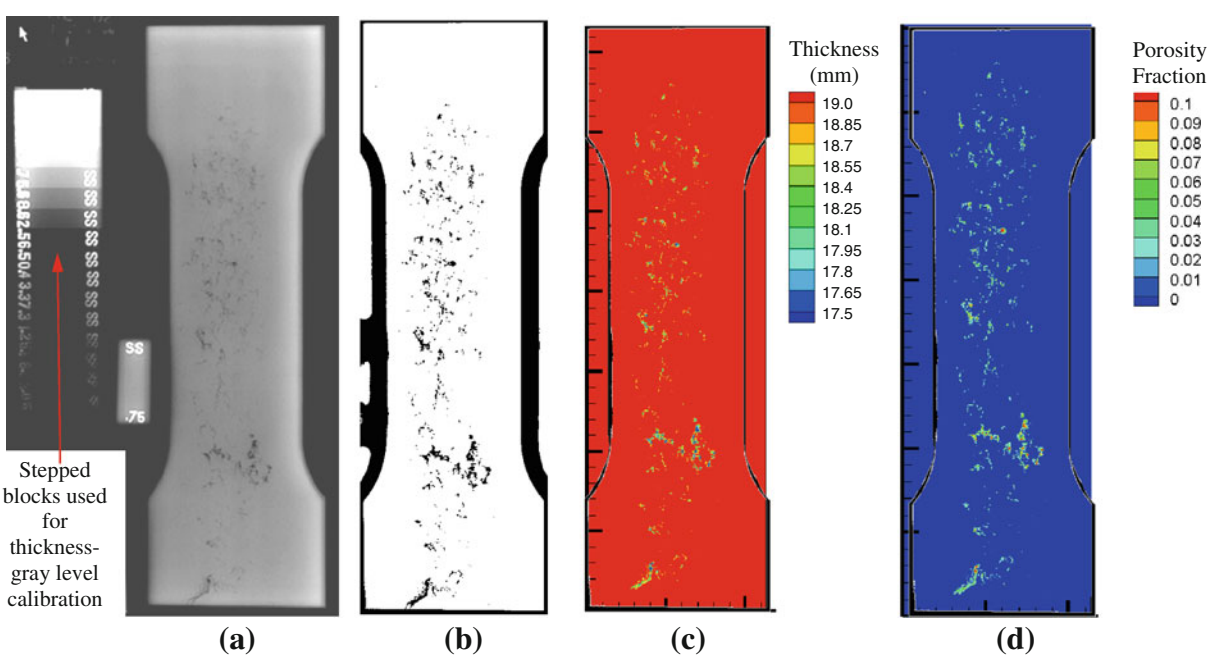

Fig. 3—(*a*) Digital radiograph of a test plate taken at 16-bit gray scale and 10 pixels per mm, (*b*) binary image of indications detected by analysis where porosity level is measured, (*c*) thickness measured at pixels with porosity and (*d*) the through-section porosity fraction measured in the test plate from the digital radiograph.

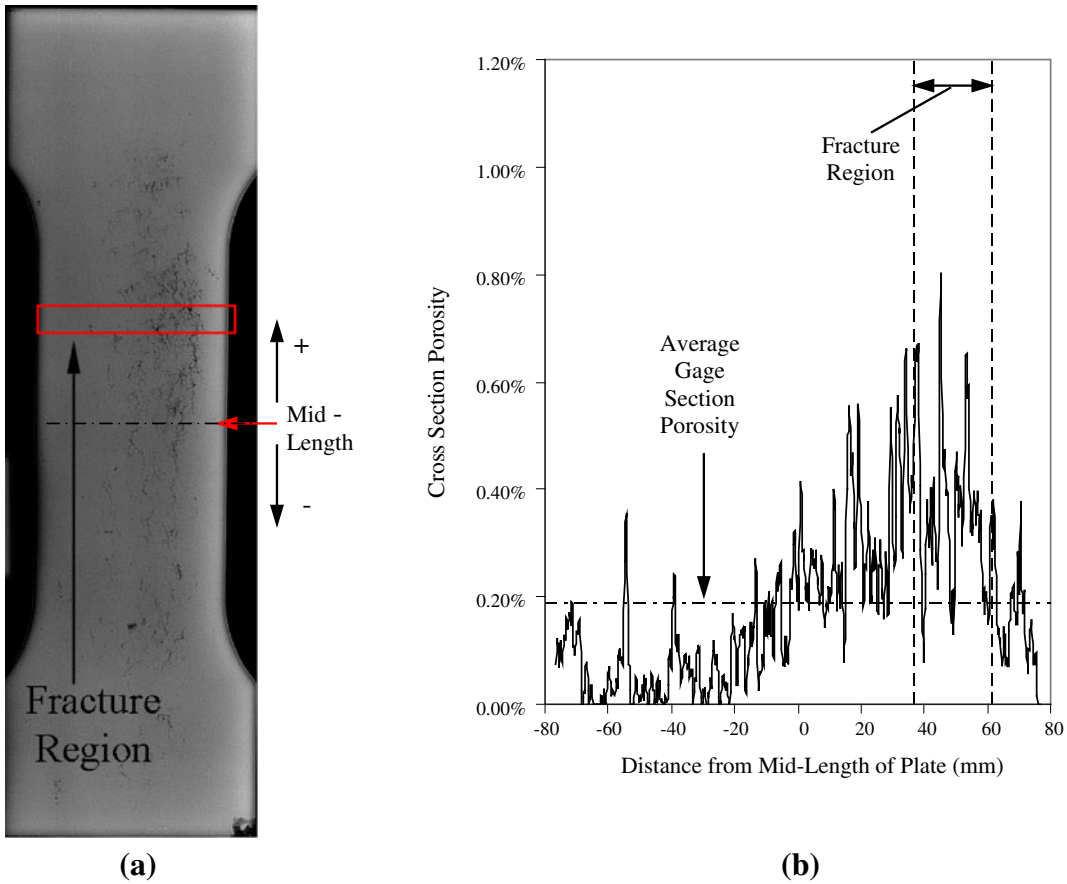

Fig. 4—(*a*) Radiograph of specimen D3 with the location of the fracture region indicated by the box. Note plate mid-length and sign convention used for distance from mid-length. (*b*) Cross section porosity along gage length of plate *vs* distance from mid-length. Note the average porosity level in the plate (0.19 pct) is indicated in addition to the region where the plate fractured.

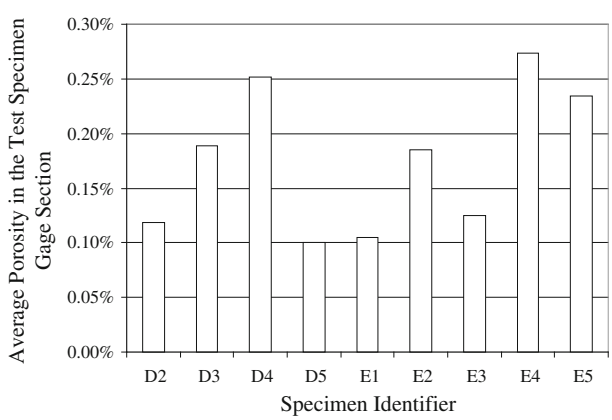

Fig. 5—Average porosity fraction measurements in the volume of the test plate gage sections determined from averaging the cross sectional porosity measurements as shown in Fig. 4(b).

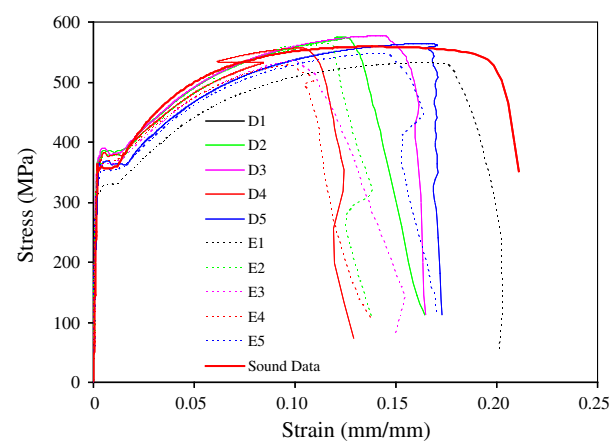

Fig. 6—Tensile testing results for sound WCB steel and the steel specimens containing centerline porosity.

with porosity on the fracture surfaces of the specimens were examined and measured to establish a reasonable assumption for the distribution of porosity in the plates. An example of a fracture surface having a region of porosity is shown in Figure 7(a), where the porosity appears to be centerline type located near the mid-thickness of the plate. Measurements of the thickness of the porosity regions were performed on the fracture surfaces to determine a reasonable thickness of porosity to use in simulating fracture of the plates. Since these regions lie on the fracture surface, they are representative of the porosity that determines the fracture behavior of the specimen. For a given region with porosity on the fracture surface, the maximum thickness dimension

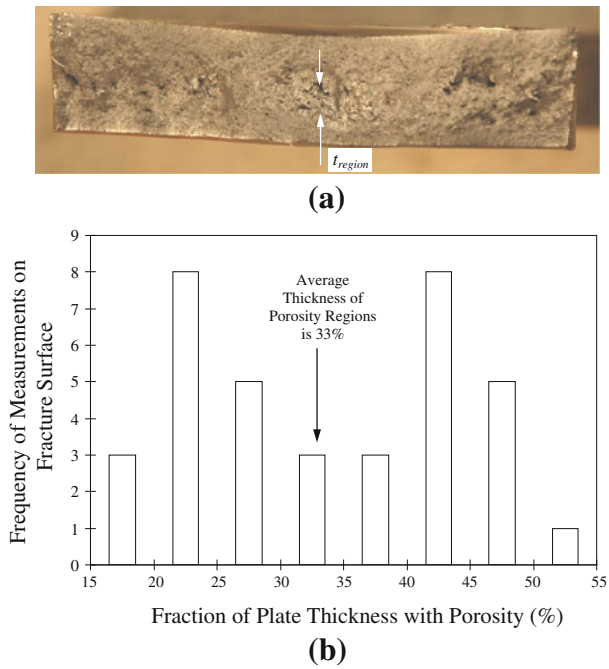

Fig. 7—(*a*) Image of fracture surface showing region with centerline porosity and measured thickness of the region, (*b*) histogram of frequencies of measured fraction of plate thickness with porosity (t_{region}/t_{plate}) on the fracture surfaces.

t_{region} of a given region of porosity was measured as shown for example in Figure 7(a). A frequency histogram of the fraction of plate thickness data corresponding to the t_{region} measurements is shown in Figure 7(b). Note that eight regions of porosity were found to fall into both the 20 to 25 pct, and the 40 to 45 pct, ranges of fraction of plate thickness. These measurements do not appear the follow a normal distribution. In Figure 7(b), the average t_{region} for all the fracture surface regions with porosity is indicated at 33 pct of the plate thickness. However, note that the bin range for the average contains relatively few observations, and might not be the best choice as a representative thickness dimension for the centerline porosity. A constant thickness of centerline porosity was assumed when reconstructing the porosity in the simulated plates. For this constant thickness, the average fraction of plate thickness with porosity from Figure 7(b) was used as a starting point in comparing predicted and measured tensile curves to establish a simulated centerline porosity thickness that would produce the best agreement. Iterative trial and error simulations were performed, varying the thickness of the simulated porosity region until the best combined agreement between measured and predicted tensile curves was found. Specimens D4 and E4 (representing the smallest measured elongation), and specimens D3 and D5 (representing the largest measured elongation) were used in these comparisons. The fracture behavior of specimen E1, which has the greatest elongation of the plates with porosity, appeared anomalous and was not used to establish the thickness of the porosity region. After these trial and error comparisons, a centerline region with porosity having 25 pct of the plate thickness was found to give the best overall agreement between the measured and predicted fracture behavior for the plates.

C. *Mapping of Measured Porosity onto Stress Analysis Mesh*

Finite element meshes of the tensile test plates were developed with mesh refinement at the plate mid-thickness to better resolve the centerline porosity as shown in Figure 8(a). The extensometer position during testing is shown in Figure 8(a). The edge of the plate where the extensometer was positioned during testing, relative to the porosity distribution in the plate, was carefully followed because of the nonuniform straining of the plate. FEA of the test plate specimens with porosity required development of a method to transfer the through-section porosity measurements determined from the radiographs onto the nodes of the FEA mesh. The porosity from the radiograph (Figure 3(d)) was mapped to the mesh assuming that it lies symmetrically about the mid-thickness of the plate in a region 25 pct of the plate thickness. A computer code was written to transfer the measurements from the radiographs to the FEA nodes where the average porosity about a nodal position in the plane of the radiograph is determined, conserving porosity. The averaging volume used about each node had dimensions of half the nodal spacing. Since this averaged porosity mapped to the FEA nodes is assumed to lie in a region 25 pct of the plate thickness, it must be scaled up by a factor $(0.25)^{-1}$ from the averaged values determined from the radiograph, where it is distributed through the entire plate thickness. Once the averaged/scaled-up porosity was determined at a nodal position, it was mapped to all nodes within the region centered at the plate mid-thickness. An example of the porosity mapping is shown for a simulated test plate on the mid-thickness plane and for a slice through the plate thickness in Figure 8(b). Comparing the porosity determined from the radiograph in Figure 3(d) to the centerline region of Figure 8(b), the porosity at the FEA nodes are diffused (caused by the averaging process about the nodes) and then amplified (due to the scaling-up at the centerline region).

III. STRESS MODELLING AND COMPUTATIONAL METHODS

A. *Material and Failure Models*

The constitutive material model used in the current study is a standard material model available in the commercial stress analysis software *ABAQUS*.[14] It assumes linear small strain theory decomposing the total strain tensor $\boldsymbol{\varepsilon}$ into elastic $\boldsymbol{\varepsilon}^{el}$ and plastic $\boldsymbol{\varepsilon}^{pl}$ components so that $\boldsymbol{\varepsilon} = \boldsymbol{\varepsilon}^{el} + \boldsymbol{\varepsilon}^{pl}$. The recoverable elastic strains of the material are calculated from

$$\boldsymbol{\sigma} = \boldsymbol{D}^{el}\boldsymbol{\varepsilon}^{el} \quad [1]$$

where $\boldsymbol{\sigma}$ is the stress tensor, $\boldsymbol{D}^{el}$ is the fourth order elasticity tensor, and $\boldsymbol{\varepsilon}^{el}$ is the elastic strain tensor.

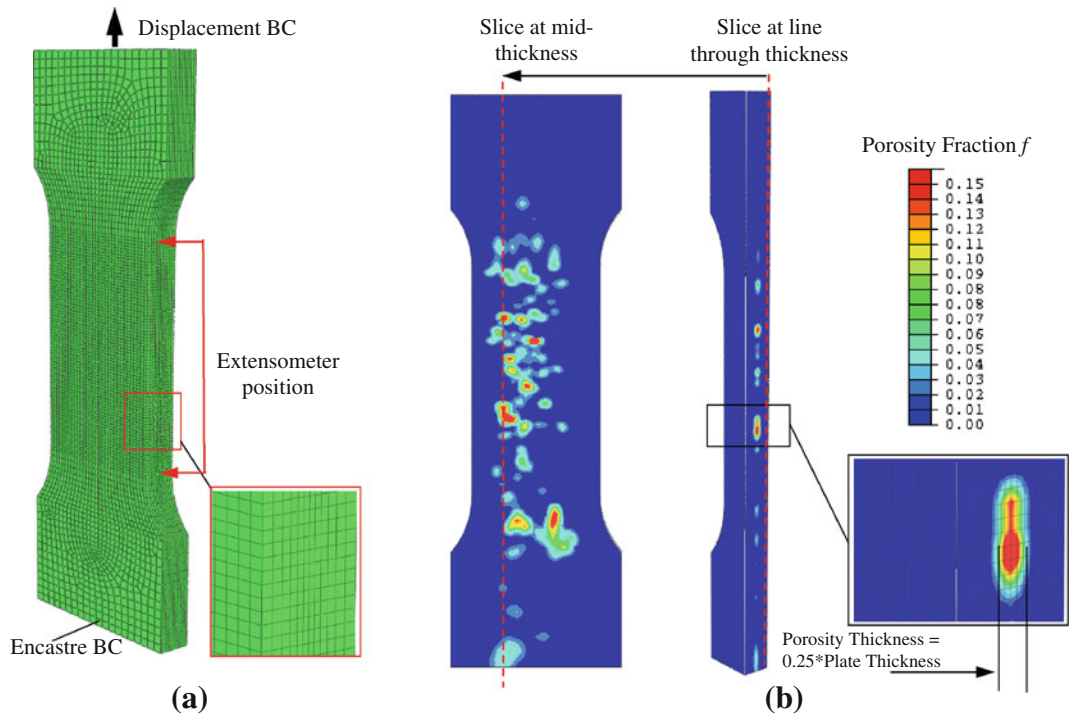

Fig. 8—(*a*) Example of a 12 element thick finite element mesh biased about the mid-thickness of a plate and (*b*) example mapping a measured porosity fraction field to the mid-thickness plane of the finite element mesh.

Note that in the case of uniaxial tension, $\boldsymbol{D}^{\mathrm{el}}$ reduces to E the elastic modulus, and Eq [1] reverts to Hooke's Law. Two properties are required to define the isotropic elasticity tensor $\boldsymbol{D}^{\mathrm{el}}$; the elastic modulus E, and the Poisson ratio v. Here the elastic material properties depend on the local porosity fraction f at the FEA nodes. The porosity fraction is $f = V_{\mathrm{pore}}/V_0$ where V_{pore} is the volume of porosity in the averaging volume about a finite element node (described in Section II–C above), and V_0 is the total averaging volume comprising voids and the steel matrix. The relationship between the elastic modulus and porosity fraction used node-by-node in the FEA analysis is

$$E(f) = E_0(1 - f/0.5)^{2.5} \qquad [2]$$

where E_0 = 198 GPa is the elastic modulus for WCB steel without porosity.[2] The Poisson ratio v is dependent on f using

$$v(f) = v_0 + \frac{f}{f_\infty}(v_\infty - v_0) \qquad [3]$$

with v_∞ = 0.14, f_∞ = 0.472 and the Possion ratio for the sound metal v_0 was 0.3. Equation [2] was determined from comparing, and achieving excellent agreement between, measured and predicted strains for cylindrical test specimens having a wide range of porosity.[2] Equation [3] was determined through simulations of computer generated representative elemental volumes of porous structures.[20] The effect of porosity on stiffness[2] was studied using locally mapped porosity at FEA nodes determined from radiography.

Here, a standard plasticity material model was used in simulating ductile plasticity and failure. A complete presentation of the model is found in Gurson *et al.*,[11–13] the software manual,[14] and the numerical integration procedure used in the software was developed by Aravas.[15] The model requires the user to define the hardening behavior of the metal matrix without porosity through true stress–strain data. This was determined from tensile tests for the sound WCB steel. The yield condition used in the model is the plastic potential ϕ given by

$$\phi = \left(\frac{q}{\sigma_y}\right)^2 + 2q_1 f \cosh\left(-\frac{3}{2}\frac{q_2 p}{\sigma_y}\right) - \left(1 + q_3 f^2\right) = 0 \qquad [4]$$

where f is the porosity fraction; q is the effective Von Mises Stress; p is the hydrostatic stress; σ_y is the yield stress of the sound steel as function of plastic strain given in Figure 9; and q_1, q_2, and q_3 are three material model parameters. In Figure 9, the plastic true stress-strain curve was derived from the measured sound steel tensile test data given in Figure 6. Note from Eq. [4] that when $f = 0$ (for porosity free material), the yield condition becomes $q = \sigma_y$, or the Von Mises yield condition, giving a yield surface that is independent of pressure. The hydrostatic stress or pressure p and the Von Mises stress q are the two stress invariants; $p = -(1/3)\,\boldsymbol{\sigma} : \boldsymbol{I}$ and $q = \sqrt{(3/2)\mathbf{S} : \mathbf{S}}$, where $\mathbf{S}$ is the deviatoric stress tensor $\mathbf{S} = p\mathbf{I} + \boldsymbol{\sigma}$.

The material parameters in Eq. [4] q_1, q_2, and q_3 were added to Gurson's original model by Tvergaard[12], and the original Gurson model corresponds to setting all the

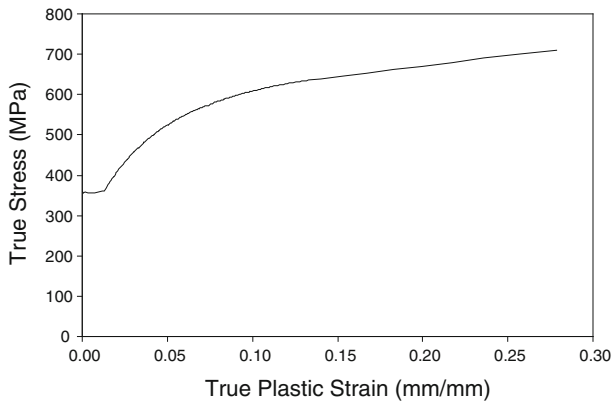

Fig. 9—True plastic stress–strain curve for ASTM A216 Grade WCB steel without porosity.

material parameters to 1. The material parameters were added by Tvergaard to consider the interactions between voids and improved the Gurson model's accuracy. In the current study, values for these parameters are used, which appear to be used often in the literature when applying the model to ductile metals;[14] $q_1 = 1.5$, $q_2 = 1.0$, and $q_3 = 2.25$, where $q_3 = q_1^2$.

Plastic flow is assumed to be normal to the yield surfaces formed by Eq. [4] for a given value of porosity fraction f. Assuming this, the yield condition of Eq. [4] is used to determine the plastic strain to grow and nucleate porosity, starting from a initial porosity fraction. As plastic strain increases, so does porosity volume fraction as will be described shortly. The flow rule determined from Eq. [4] for the plastic strain rate $\dot{\boldsymbol{\varepsilon}}^{\mathrm{pl}}$ tensor is

$$\dot{\boldsymbol{\varepsilon}}^{\mathrm{pl}} = \dot{\lambda}\frac{\partial\phi}{\partial\boldsymbol{\sigma}} = \dot{\lambda}\left(-\frac{1}{3}\frac{\partial\phi}{\partial p}\mathbf{I} + \frac{3}{2q}\frac{\partial\phi}{\partial q}\mathbf{S}\right) \qquad [5]$$

where $\dot{\lambda}$ is a nonnegative scalar constant of proportionality for the plastic flow rate. Given that the plastic strain in Eq. [5] causes porosity growth and nucleation as it increases, the equation describing the growth rate of porosity voids by growth and nucleation is

$$\dot{f} = (1-f)\dot{\varepsilon}_{\mathrm{kk}}^{\mathrm{pl}} + A\dot{\varepsilon}_{\mathrm{m}}^{\mathrm{pl}} \qquad [6]$$

where the first term on the right hand side denotes growth of existing voids from current porosity fraction f and $\dot{\varepsilon}_{\mathrm{kk}}^{\mathrm{pl}}$ the total plastic strain rate (trace of the strain rate tensor), and the second term denotes the growth rate due to nucleation. In the nucleation term, the equivalent plastic strain rate $\dot{\varepsilon}_{\mathrm{m}}^{\mathrm{pl}}$ is multiplied by a scaling coefficient

$$A = \frac{f_{\mathrm{N}}}{s_{\mathrm{N}}\sqrt{2\pi}}\exp\left[-\frac{1}{2}\left(\frac{\varepsilon_{\mathrm{m}}^{\mathrm{pl}} - \varepsilon_{\mathrm{N}}}{s_{\mathrm{N}}}\right)^2\right] \qquad [7]$$

based on the assumption that the nucleation function (A/f_{N}) follows a normal distribution depending on the plastic strain range about a mean value ε_{N}, a standard deviation s_{N}, and a volume fraction of nucleated porosity voids f_{N}. Using the void nucleation model requires fitting these three parameters for a given material's tensile curve. Here values in the range recommended for metals were used:[14] $\varepsilon_{\mathrm{N}} = 0.3$, $s_{\mathrm{N}} = 0.1$, and $f_{\mathrm{N}} = 0.03$ and these have good agreement with the sound WCB steel tensile curve. The effect of varying f_{N} on the predicted tensile curve will be presented shortly.

Table I. Parameters Used in the Porous Metal Plasticity Model for WCB Steel in *ABAQUS* Simulations

q_1	q_2	q_3	f_0	f_{c}	f_{F}	ε_{N}	s_{N}	f_{N}
1.5	1.0	2.25	0.005	0.05	0.2	0.3	0.1	0.03

Coalescence and failure modeling extends the porous metal plasticity model to higher levels of porosity than the range of Gurson's original model, which is less than 10 pct. The coalescence and failure criteria used here were developed by Needleman and Tvergaard[13] where the porosity fraction f in Eq. [4] is replaced by an effective porosity volume fraction due to coalescence f^*. In Eq. [4], f^* takes on the actual porosity volume fraction f when it is less than the critical value f_{c}, where coalescence begins. Therefore, for values of $f < f_{\mathrm{c}}$, $f^* = f$. When $f^* > f_{\mathrm{c}}$ the effective porosity fraction increases more rapidly than f because of the coalescence. This coalescence is modeled by increasing f^* by a factor of $(\bar{f}_{\mathrm{F}} - f_{\mathrm{c}})/(f_{\mathrm{F}} - f_{\mathrm{c}})$ relative to the increase in f. The material has no load carrying capacity when $f \geq f_{\mathrm{F}}$, where f_{F} is the porosity fraction at failure. The equations describing the dependence of f^* on f where f^* is used in place of f in Eq. [4] are

$$f^* = \begin{cases} f & \text{if } f \leq f_{\mathrm{c}} \\ f_{\mathrm{c}} + \frac{\bar{f}_{\mathrm{F}} - f_{\mathrm{c}}}{f_{\mathrm{F}} - f_{\mathrm{c}}}(f - f_{\mathrm{c}}) & \text{if } f_{\mathrm{c}} < f \leq f_{\mathrm{F}}, \\ \bar{f}_{\mathrm{F}} & \text{if } f \geq f_{\mathrm{F}}, \end{cases} \qquad [8]$$

The value of $\bar{f}_{\mathrm{F}}$ in Eq. [8] is set using the "q" porous metal plasticity model material parameters by

$$\bar{f}_{\mathrm{F}} = \frac{q_1 + \sqrt{q_1^2 - q_3}}{q_3} \qquad [9]$$

There are two additional parameters that must be determined when using the coalescence and failure model: f_{c} and f_{F}, the critical and failure porosity fractions, respectively. Here, these values were determined by fitting the model fracture curve to the measured curve for sound WCB steel. The values giving the best agreement were $f_{\mathrm{c}} = 0.05$ and $f_{\mathrm{F}} = 0.2$, and the effect of varying f_{F} on the predicted tensile curve will be discussed below. To summarize, the nine model parameters used in the porous metal plasticity model here are given in Table I, and these give the best agreement found between the predicted and measured tensile curves. The model described here is intended to give the most important model features and the parameters used. Additional details on the model and the solution scheme are given in References 11 through 16.

B. *Finite Element Modeling*

The boundary conditions used in the simulations of the tensile testing of the plates were an encastre condition on the base of the specimen and a normal displacement applied to the top surface of the specimen as shown in Figure 8(a). The simulated testing load was given by the total force on the wire element used to apply the displacement boundary condition. As mentioned earlier, the edge of the specimen where the extensometer was positioned during testing was marked on each specimen, and that edge was used to extract the simulated testing strains. This was done in case the porosity field resulted in differences between the two edges of the specimen. Simulated extensometer strains presented in the stress–strain plots that follow were determined from the displacements of node sets defined at the extensometer knife-edge positions as shown in Figure 8(a).

In order to use the failure criterion in the porous metal plasticity model, *ABAQUS Explicit* was used to perform the fracture simulations. Two considerations are important when applying an explicit procedure to a quasi-static process such as the tensile testing simulations. The first is the time period of the tensile test event. While the actual testing might require on the order of a minute, the simulated event can be modeled over a much smaller time scale without the results changing. The second consideration is the stable time increment which is dependent on the smallest characteristic element length in the mesh and the dilatational wave speed of the material. The stable time increment issue was examined first, and then the event time period was determined, so that the simulations could be executed in a reasonable number of increments without the results being affected. The wave speed in steel c_d is about 5,000 m/s, given by $\sqrt{E/\rho}$ where ρ is the density. The largest stable time step Δt_{stable} that can be taken in an explicit dynamics calculation is given by $\Delta t_{\text{stable}} = L_{\text{e}}/c_{\text{d}}$, where L_{e} is the smallest characteristic element length. For characteristic element lengths ranging from 0.7 to 4 mm, the largest stable time step range is 1.4 to 8.0×10^{-7} s. If the tensile testing event were to be simulated on its actual time scale, then the simulations would require 10 s of millions of time steps and would be impractical. A practical time scale for the testing event was established by considering the time the stress wave transmits through the test specimen and multiplying it by a safety factor that is sufficiently large. The specimen is 318 mm long, and the time to transmit a stress wave through the specimen is about 6×10^{-5} s. A multiplying safety factor between 10 and 100 times the transmission time would be probably be an adequate event length, but a multiplying factor of over 1000 times was used. The time period used for the tensile testing event in the simulations was 0.085 s. Experimenting with smaller and larger event periods confirmed the event duration did not affect the results. Another check on the rates of the simulated of loading performed was a comparison between the velocity of the displacement of the testing and the wave speed. Based on the tensile event being 0.085 s long, the test specimen end displacement speed is about 0.53 m/s. While this displacement speed seems high, it is only 0.01 pct of the material's wave speed. As another final check, the kinetic and internal energies of the model were stored during simulation runs to confirm that the kinetic energy did not exceed approximately 5 pct of the internal energy as per the software's guidelines for simulating quasi-static processes. It was found that the kinetic energy did not exceed 0.6 pct of the internal energy.

Unless otherwise noted in the simulations in the computational results section presented here, the FEA mesh employed in the length and width directions of the gage section had a uniform nodal mesh spacing of 1 mm. Nonuniform meshes through the plate specimens' thickness were used in simulating the final results for all the specimens, where the mesh had smaller elements biased toward the centerline as seen for example in Figure 8(a). In that figure, the mesh is shown for demonstration purposes and has 12 elements across the plate thickness. In computational models used to generate results reported here, 20 elements were used across the plate thickness with a bias factor of 3. The FEA model used to generate final results presented here had 379,681 C3D8 elements, 403,878 nodes, and the total number of variables was 1,213,081. These simulations required about 663,212 increments and approximately 4 days and of computer time using eight cores of a Linux workstation with 16GB ram, and two Intel Xeon CPU E5472 CPUs running at 3.00 GHz. For the finest mesh case used in the grid sensitivity study to be described later, the "0.7-mm mesh spacing" results having 30 elements across the plate thickness and using centerline-biased elements, very small characteristic element lengths required the use of the mass scaling option, "*FIXED MASS SCALING," which increases the density of elements if their stable time increment is smaller than a specified increment. The specified time increment for those elements was chosen such that the total number of increments was limited to about 2.8 million.

IV. COMPUTATIONAL RESULTS

A. *Results for Sound Material and Determination of Constitutive Material Model Parameters*

Simulations were first run using "sound" steel to determine the nine porous metal plasticity model parameters given in Table I. After these model parameters were determined by matching the predicted and measured fracture behavior of the sound material, the plates with porosity were simulated. The porous metal plasticity parameters were not changed when simulating the plates with porosity; only the mapped porosity field for each plate was added to the simulation input when simulating the plates with porosity.

The porous metal plasticity model material parameters given in Table I were determined by matching the measured and predicted tensile curves and fracture

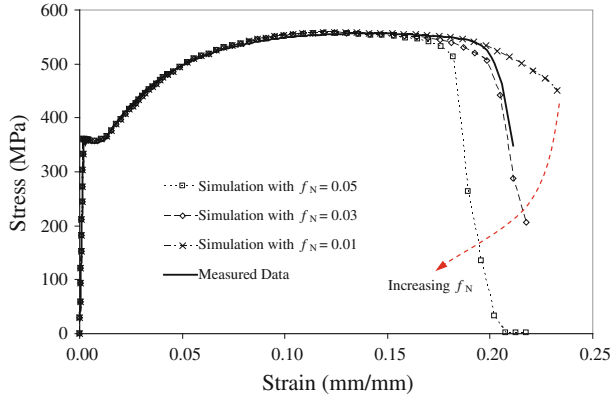

Fig. 10—Effect of varying the nucleation porosity fraction f_N on the predicted tensile curves compared with the measured curve.

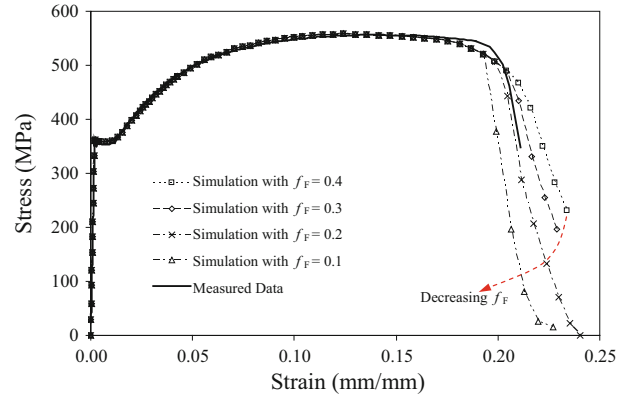

Fig. 11—Effect of varying the failure porosity fraction f_F on the predicted tensile curves compared with the measured tensile curve.

behavior. It was determined that the "q" model parameters should not be changed from recommended values.[14] The sensitivity of the fracture curve to the remaining six parameters were examined and varied by trial and error to achieve the best agreement that could be obtained between the measured and predicted fracture curves. Examples of the sensitivity of the simulated tensile curves to two of the parameters are given in Figures 10 and 11 for the nucleation porosity fraction f_N and the failure porosity fraction f_F, respectively. Increasing the void nucleation fraction from 1 to 5 pct progressively decreases the predicted elongation and results in a less ductile material behavior as seen in Figure 10 for the 5 pct curve. A nucleation fraction of 0.03 was found to give the best agreement overall for f_N. The effect of varying the failure porosity fraction f_F is shown in Figure 11, where it is increased from 10 to 40 pct. The larger the failure porosity fraction is the greater the elongation. A failure porosity fraction of 20 pct was found to produce the best agreement between predicted fracture behavior and that observed in testing for f_F. The measured and best predicted sound steel curves are given in Figure 12 with model material parameters from Table I used to produce the simulated curve. For the sound material, the maximum elongation at failure, ultimate tensile stress, and yield stress are predicted within 2 pct. The agreement between the sound curves is good and represents best possible agreement that would expected between predicted and measured curves for the specimens with porosity. Since the elongation at fracture cannot be determined from the simulations by reassembling the fractured specimen, a common point of reference along the tensile curves was chosen to compare the predicted and measured strain at fracture. For the measured sound curve in Figure 12, the last stress measured in the test during fracture was 348 MPa. This also corresponds to a point of nearly perfect agreement between the measured and predicted sound steel curves. Since it provides a good basis for comparison for the sound material, as indicated in Figure 12, the strains at this 348 MPa stress level were used to compare the measured and predicted elongation for all the fracture specimens with porosity as well.

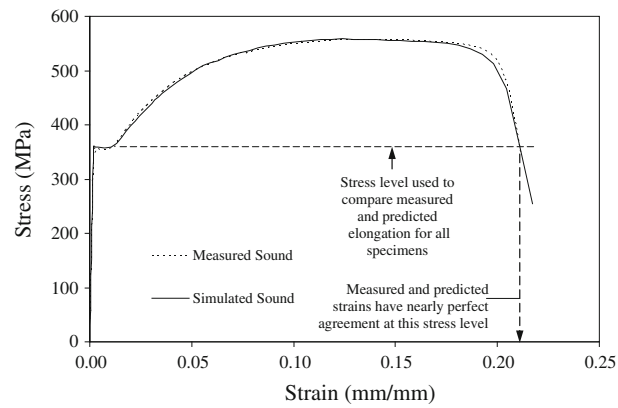

Fig. 12—Simulated and measured stress–strain curves for the sound WCB steel. The stress level at which measured and predicted elongation are compared for all plates is indicated.

B. *Simulations of Steel with Centerline Shrinkage Porosity*

The dependence of simulation results on computational mesh density was investigated to confirm converged results. Several of the plates with porosity were studied to determine that the mesh used would be fine enough to achieve grid independency in the mapping of the porosity to the computational mesh. Consider plate E4 in Figure 13, where its radiograph is shown in Figure 13(a). In Figures 13(b) trough (e), mid-thickness sections of the porosity fraction for four nodal mesh spacings are shown, having spacings of 4 mm, 2 mm, 1 mm, and 0.7 mm, respectively. For the 0.7-mm mesh, 30 elements were generated across the specimen thickness using biasing of elements at the mid-thickness. For the 4-mm, 2-mm, and 1-mm mesh spacings, uniform meshes in the specimen thickness direction were used having 6, 12, and 20 elements in the thickness direction, respectively. In Figure 13, note the porosity field is more diffuse with coarse meshes and that the maximum nodal porosity value (shown for each field in Figure 13) ranges from 34 pct for the coarsest mesh to 52 pct for the finest mesh. A white-boxed area is shown for each mesh,

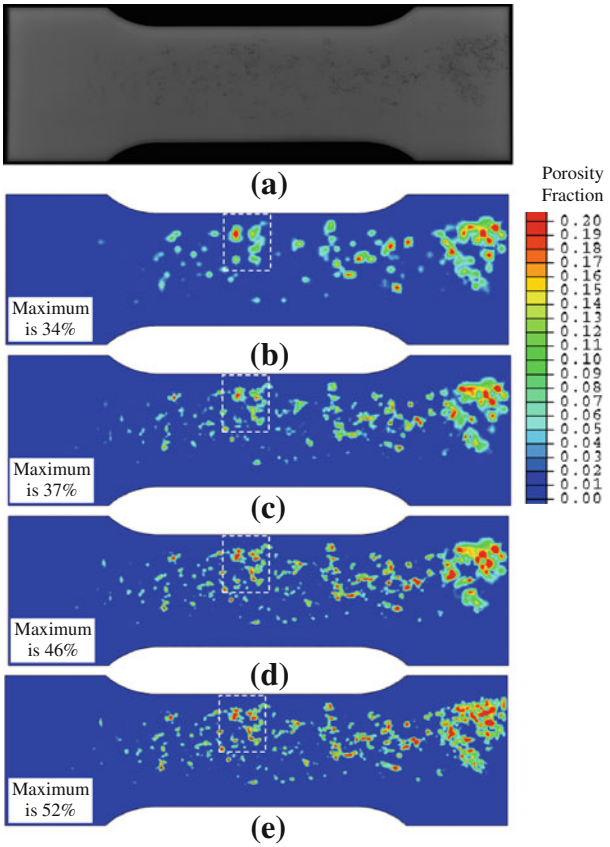

Fig. 13—(*a*) Radiographs of plate E4, and porosity fraction at mid-thickness plane for four meshes used in simulation grid dependency studies for plate E4 having the following mesh spacings in the gage section: (*b*) 4 mm, (*c*) 2 mm, (*d*) 1 mm, and (*e*) 0.7 mm. White-dashed boxed areas in gage section are shown for more a detailed comparison in Fig. 14.

which is shown in more detail in Figure 14, along with the corresponding area from the radiograph in Figure 14(a). In the detailed view, the porosity fields for the two fine meshes (in Figures 14(d) and (e) are nearly identical, and the porosity mapping process appears to be mesh independent for the finest meshes. The measured tensile curve for specimen E4, and the simulated tensile curves for the four mesh densities are shown in Figure 15, along with two additional simulated mesh spacings of 3 and 2.5 mm. For meshes coarser than the 1-mm spacing, it is found that the simulated curves have greater elongation with increasing mesh spacing up to 3- and 4-mm mesh spacings. There is no great difference between the 3- and 4-mm tensile curves. The simulated tensile curves for the 0.7- and 1-mm mesh spacings appear to converge together and agree well with the measured curve. Based on this grid convergence study, the 1-mm mesh spacing was used to simulate the plates. The 0.7-mm mesh spacing with 30 elements through the plate thickness required approximately 1 week of computational time on the machine referred to earlier, and this was too long a computational time to use in simulating all the specimens.

The tensile curves for the plate specimens with porosity were simulated using the centerline porosity fields mapped to the FEA nodes at the plates' mid-thickness. Plates with porosity were simulated using the model parameters in Table I, and where there is no nodal porosity mapped from the radiograph, the porosity is 0.5 pct. As shown in Figure 4, the average fraction of plate thickness with porosity was found to be 33 pct. In general, it was found that using 33 pct of the plate thickness as the centerline porosity thickness (as in Figure 7) gave greater elongation predictions than observed in testing. If a single value for the centerline porosity thickness is used for all plates, the best agreement overall between the measured and predicted fracture behavior was found using 25 pct of the plate thickness. As discussed earlier, this choice was based on simulating the tensile curves for specimens D4, E4, D3, and D5, measured curves of which are given in Figure 6. Similar to the grid dependency study, a centerline porosity region thickness study was performed using the 1-mm uniform mesh which gives a grid independent result in Figure 13. Because of the days required to simulate a tensile curve, it was decided to do a thorough study using only plate E4 for the range of porosity region thickness measurements taken from the fracture surfaces plotted in Figure 7. Considering that the smallest thickness dimension measured from the fracture surface was about 15 pct, a simulation case for a 10 pct plate thickness of centerline porosity was run as well to test a thickness that was much smaller than what was observed. The tensile curve results for the centerline porosity region thickness study are shown in Figure 16, where the measured curve for specimen E4 is shown for comparison. The porosity region thicknesses used were 10, 20, 25, 30, 40, and 50 pct of the plate thickness. Note that as the porosity region thickness is increased the porosity fraction within the region decreases and *vice versa*. The tensile curve for the 10 pct porosity thickness has an unrealistically large elongation. Indeed, a case was run (but not shown here) where the porosity was assumed to be a complete hole of varying thickness corresponding to the measured porosity, and that tensile curve even more closely approached the curve for the sound material. The porosity thickness study results show that as the thickness increases from 10 to 50 pct the ductility of the simulated material decreases. The measured curve appears to be bracketed by the 20 and 30 pct of plate thickness curves, and the 25 pct tensile curve appears to agree best with the measured one. Based on these results and additional simulations for specimens, D4, D3, and D5 which showed similar agreement, 25 pct of the plate thickness was chosen as the porosity region thickness in the simulations. As a final remark, unrealistically large values of assumed porosity region thickness were found to give unrealistically large elongations. A plate was simulated where the porosity was taken as uniform through the entire plate thickness and the resulting tensile curve had a large elongation approaching that of the sound material.

In Figure 17, the measured and predicted tensile curves for plate E4 is shown. The reduction in ductility due to the porosity and fracture behavior is well predicted when one compares it to the sound curve. In Figure 17, three points along the tensile curve are indicated to demonstrate the progressive behavior of the failure process within the plates with porosity. The

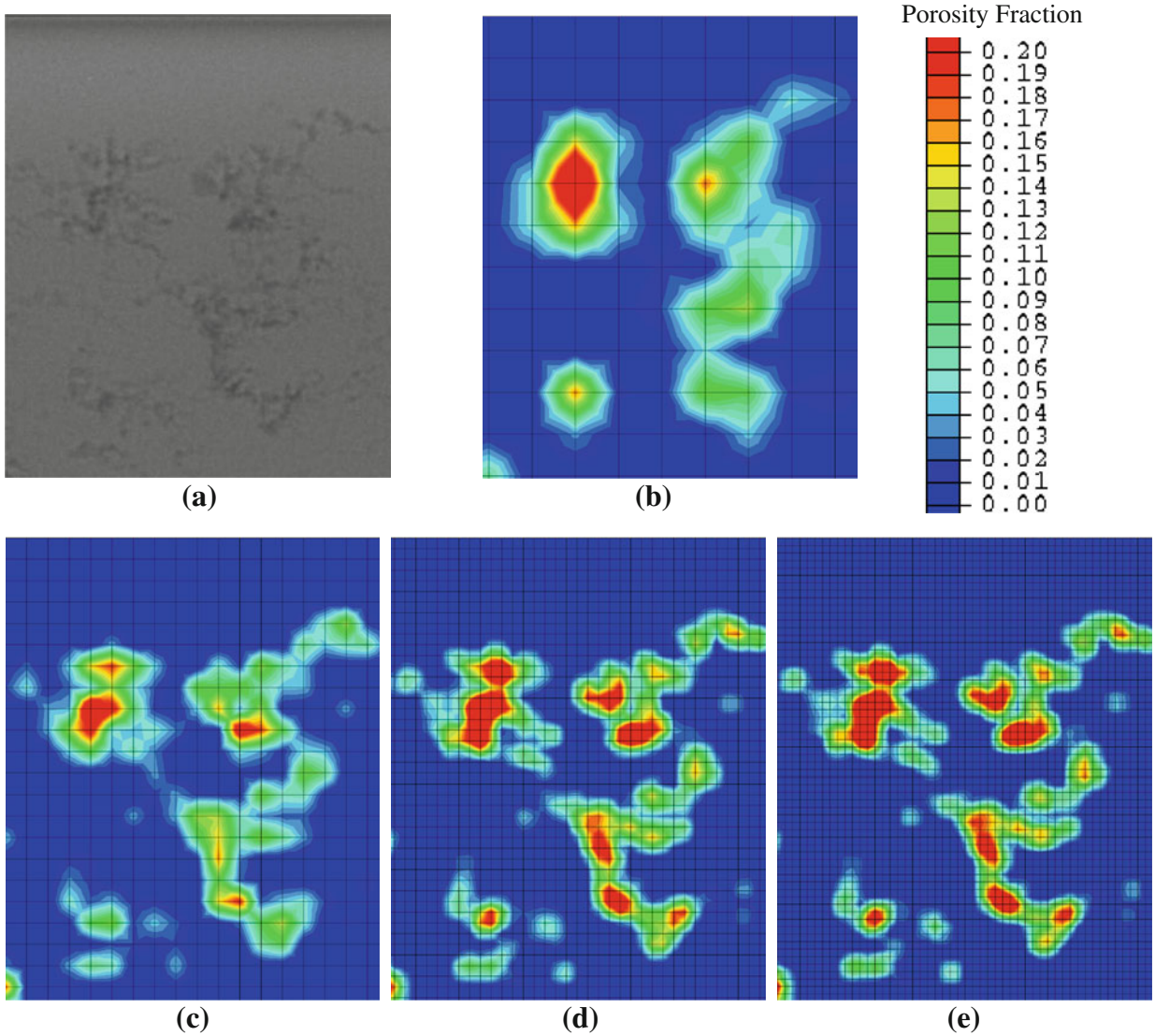

Fig. 14—(*a*) Radiograph of area for detailed comparison of porosity fraction indicated in Fig. 13 for four meshes used in the grid studies. Porosity fraction at mid-thickness in the radiograph area for nodal mesh spacings of (*b*) 4 mm, (*c*) 2 mm, (*d*) 1 mm, and (*e*) 0.7 mm.

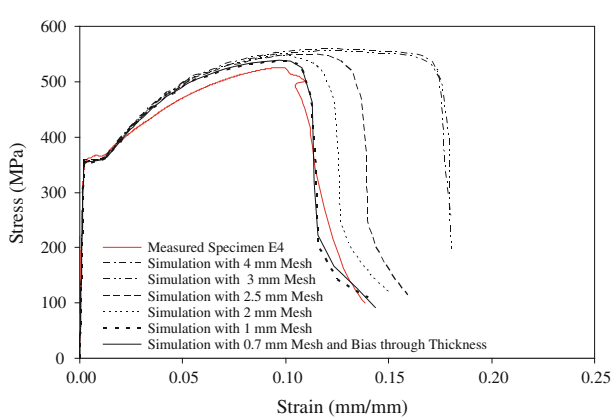

Fig. 15—Tensile curves from grid dependency studies for a plate with porosity using uniform meshes having dimensions 4, 3, 2.5, 2, 1, and a 0.7-mm spacings having a biased mesh in the plate thickness direction to concentrate nodes at the centerline. Measured curve is also shown. Centerline porosity thickness used is 25 pct of the plate thickness.

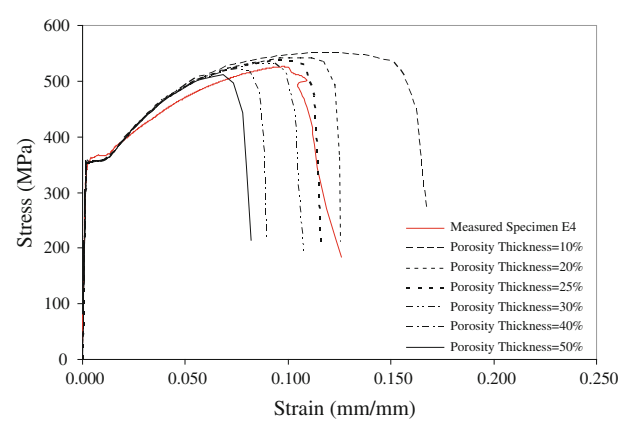

Fig. 16—Tensile curves for plate E4 for assumed thickness of centerline porosity as fraction of plate thickness in percent. Measured curve and curves for centerline porosity region thicknesses of 10, 20, 25, 30, 40, and 50 pct of the plate thickness are shown. The grid used is the 1-mm uniform mesh from the grid dependency study in Fig. 15.

testing strain is approximately 0.002, 0.045, and 0.104 at Points 1, 2, and 3, respectively. The plastic strain and porosity fraction results at the mid-thickness of the plates are of particular interest since the porosity located there determines the overall tensile response and the failure. Note that Point 1 is still in the elastic portion of the tensile curve, Point 2 is about midway through the plastic region, and Point 3 is at the position of ultimate tensile strength just before the onset of failure. The equivalent plastic strain results at these three points are shown in Figure 18. Note that even in the elastic part of the curve at Point 1, there is plastic strain occurring because of and near to the porosity. In Figure 19, the porosity fraction at the mid-thickness of the plate is shown where the scale is chosen to demonstrate the porosity fraction increasing until failure occurs. In Figure 19, the results for porosity fraction at Point 1 are virtually unchanged from the initial porosity field (not shown). From Point 1 to 3 the porosity fraction increases because of void growth and nucleation until failure occurs. The scale in Figure 19 was set to 0.15 maximum porosity fraction to accentuate the areas where porosity evolves. Recall though that the material failure occurs at 20 pct porosity fraction. Positions of observed and predicted failure are noted in Figure 19. The position of predicted final failure corresponded to the position along the plate length where the tested specimen failed.

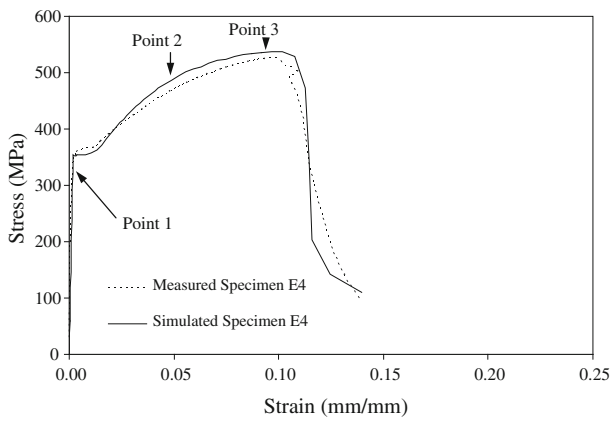

Fig. 17—Simulated and measured stress–strain curves for the specimen plate E4 with porosity. Three points of interest along the tensile curve are indicated.

White-dashed boxed areas in gage sections of Figures 18 and 19 are shown for more a detailed comparison in Figure 20. Figure 20(a) shows the equivalent plastic strain field and mesh and 20(b) the porosity fraction. Considering these fields, the material's behavior

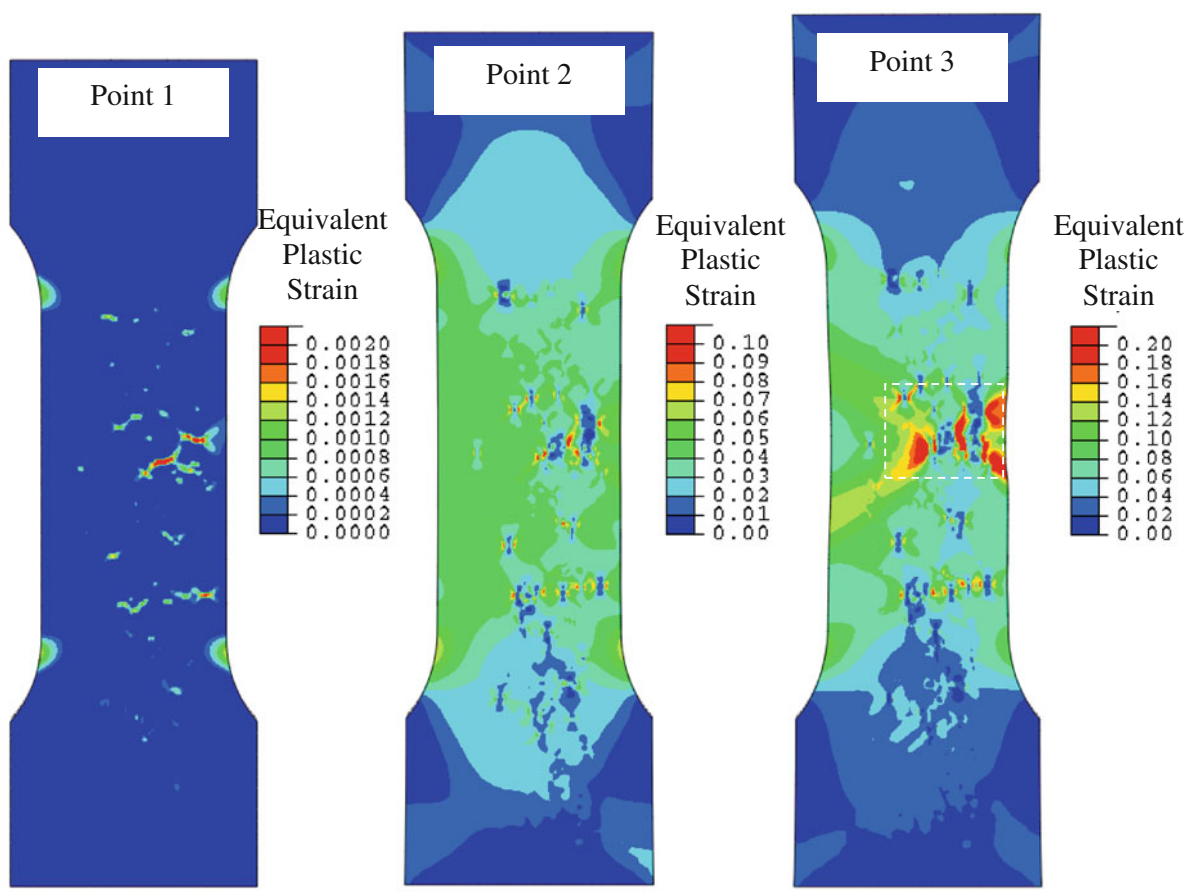

Fig. 18—Equivalent plastic strain from simulation at the mid-thickness plane of plate E4 for the three points on the tensile curve indicated in Fig. 17. The legend scales are increasing from Point 1 to 3. Note there is local plastic straining in the elastic portion of the curve at Point 1. A white-dashed boxed area in the gage section at Point 3 is indicated for a more detailed examination in Fig. 20.

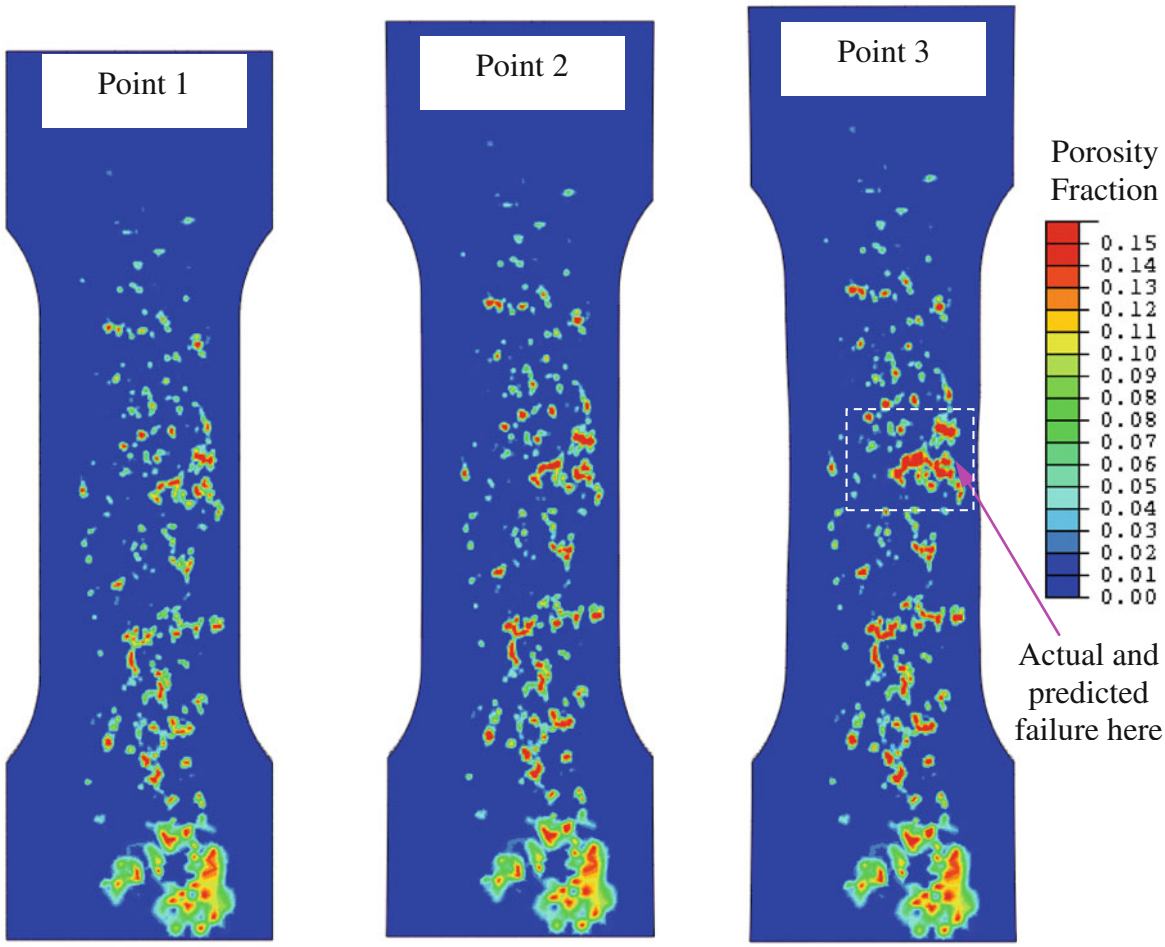

Fig. 19—Simulation results for porosity fraction at plate E4 mid-thickness at the three points on the tensile curve indicated in Fig. 17. The porosity fraction damage increases until failure occurs. Position of final failure is indicated. At Point 3 a white-dashed boxed area in gage section is indicated for more a detailed comparison with the equivalent plastic strain in Fig. 20.

can be quite different depending on how the porosity is distributed relative to the load. In Figure 20, the loading direction is indicated. In the figure, it is demonstrated that in some sound areas neighboring the porosity, there is higher equivalent plastic strain because of that sound material bearing more of the load, and these areas are indicated by the four white "▲" symbols. They bear more load because of the porosity reducing the cross section normal to the load. However, these areas can only bear the load provided they have continuous regions without porosity along the loading direction (above and below them). If this occurs, and they are surrounded by porosity, then the sound regions are isolated from bearing the load and have a low plastic strain. The white symbol "●" indicates a sound region that **is** isolated from bearing the load by two surrounding areas of porosity above and below it. At Point 3 in Figures 19 and 20(b), it is apparent why the simulation predicts failure where it does, since the porosity regions are becoming interconnected. Note the distorted/failed elements that are seen in detail in Figure 20(b). Figure 21 is provided to show the simulated development of average porosity in gage section of test plate E4 and predicted stress as functions of simulated extensometer strain during tensile testing. As seen by the solid curve in Figure 21, the initial average porosity in the plate gage section is about 0.75 pct and increases slowly until the ultimate tensile stress is reached, after which it increases rapidly because of the failure event. These results give additional insight into the model, and the complexity of the interaction between the porosity and the elastic–plastic model, and the resulting nonuniform stress and strain fields.

Figure 22(a) is provided to show the simulated and measured tensile curves for a second plate, D2. Here again the reduction in ductility and fracture behavior is reasonably well predicted. During testing of specimen D2, the control system stopped the test before complete fracture, and thus the appearance of the specimen just before complete failure was captured in Figure 22(b). This photo of the plate after testing in Figure 22(b) compares favorably with the predicted appearance of the final failure in Figure 22(c). In comparing Figures 22(b) and (c), note the circled regions where the final material failure occurs during testing. This interesting correspondence might have been missed if the plate had completely fractured. If the current study were to be repeated, then comparing the simulation

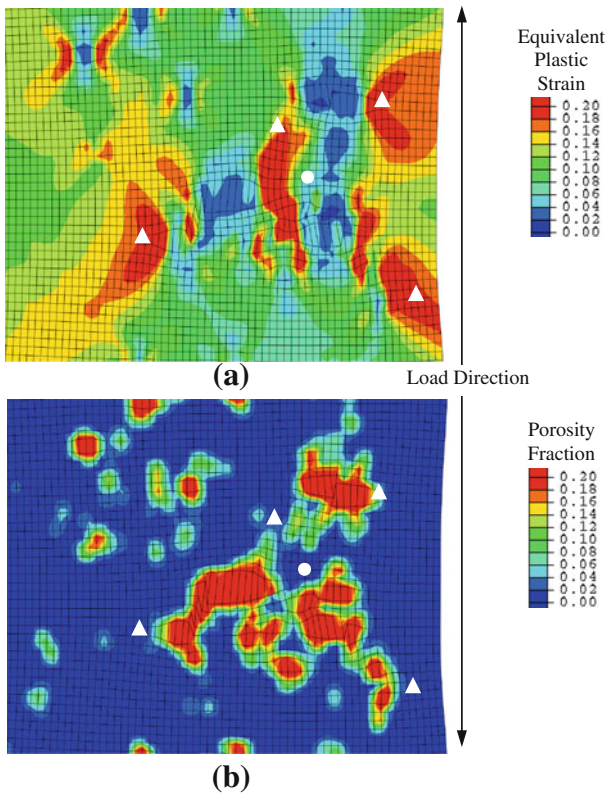

Fig. 20—Simulation results for (*a*) equivalent plastic strain and (*b*) porosity fraction for plate E4 at mid-thickness and Point 3 on the tensile curve indicated in Fig. 17. Area is the white-dashed boxed areas indicated in Figs. 18 and 19. The white symbol "●" indicates a sound region that is isolated from the loading by surrounding porosity, and it bears little of the load. The four white "▲" symbols indicate sound regions that are bearing large loads and large plastic strains. These areas have uninterrupted sound material in the loading direction.

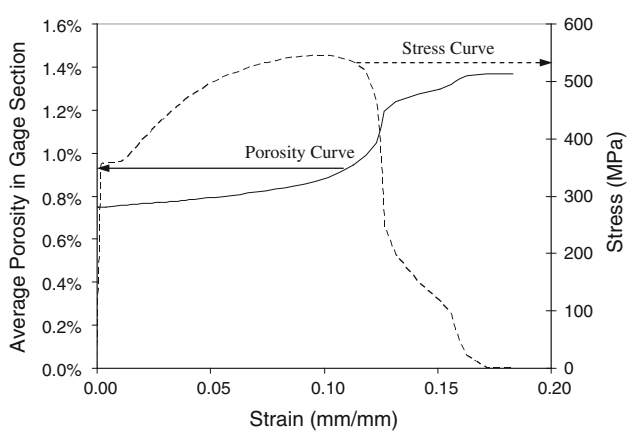

Fig. 21—Simulated development of average porosity in gage section of test plate E4 and stress as functions of extensometer strain during tensile testing.

animations with a video record of the testing and failure events could provide additional evidence supporting this modeling approach.

In lieu of presenting all the fracture curves for the nine plates with porosity, the predicted and measured

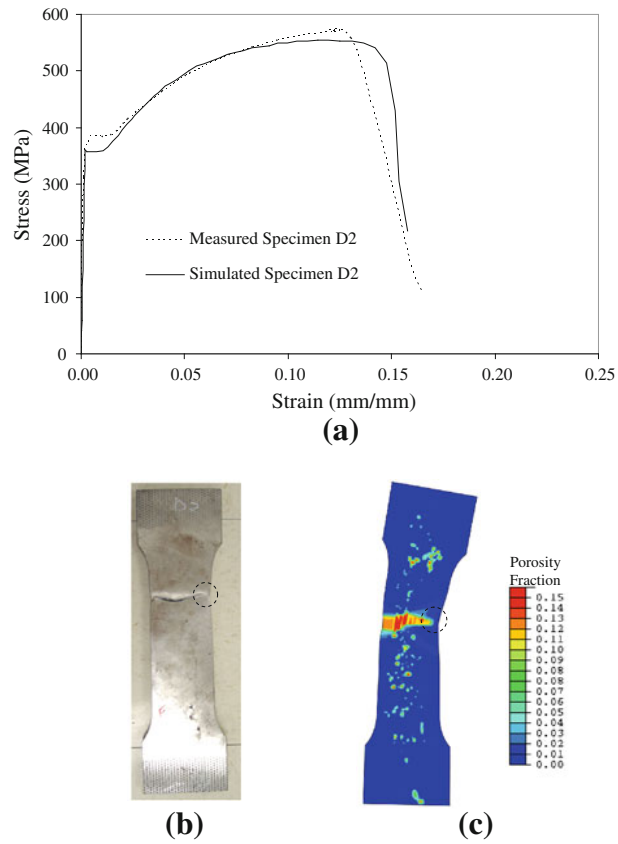

Fig. 22—Results for plate D2 (*a*) predicted and measured tensile curves, (*b*) photo of plate after testing, and (*c*) simulated porosity on mid-thickness plane at fracture.

elongation results from the fracture curves at the 348 MPa testing stress level (shown in Figure 12) are given for all the specimens tested in Figure 23. The sound elongation data point is circled and demonstrates nearly perfect agreement since the model parameters were tuned to achieve this agreement. Ductility in the test castings with porosity is markedly reduced with the percent elongation data ranging from 12.8 to 19.6 pct; *vs* 22 pct elongation for the sound material. The results in Figure 23 demonstrate the success of this modeling approach to predict the effect of porosity on the fracture behavior despite a key assumption: that the centerline porosity is positioned at the plate mid-thickness, having a thickness dimension of 25 pct of the plate thickness. The elongation results demonstrate that the main outlying data point is Specimen E1, where the measured elongation is underpredicted. The measured elongation for Specimen E1 is 19.6 pct, and as was noted earlier, referring to Figure 6, its measured tensile curve was quite different from the other specimens. From the porosity thickness study summarized in Figure 16, the behavior of specimen E1 could be explained if the porosity distribution through the thickness of plate E4 is more concentrated at the centerline relative to the other plates. Using a smaller fraction of the plate thickness for the porosity thickness will improve the comparison between the simulation and measurement for E1, since the predicted elongation will be greater. Even so, as

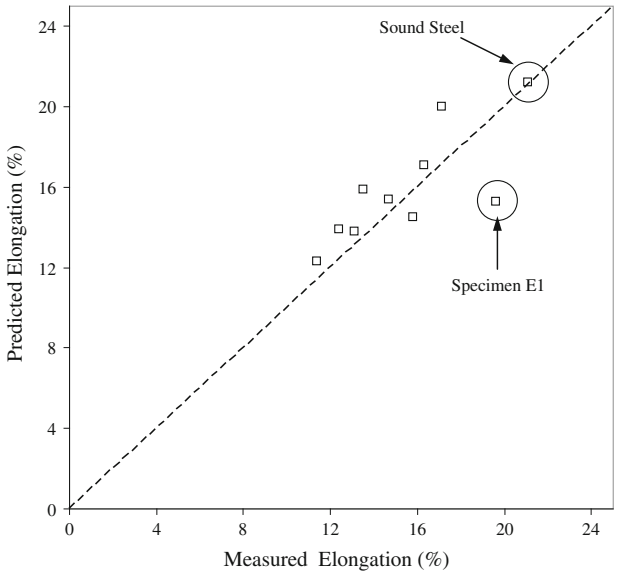

Fig. 23—Predicted *vs* measured elongation for sound WCB steel (circled) and for plates with porosity. Result for specimen plate E1 is also circled.

summarized in Figure 23, the methodology presented here for predicting the fracture behavior of a casting with centerline porosity using analysis of radiographs and porous metal plasticity in FEA appears validated. By improving the realism of the porosity reconstruction and mapping in the simulation, through X-ray tomography, for example, the assumption employed here on the distribution of centerline porosity can be removed. Upon doing this, the validity of the modeling approach could be judged with greater certainty.

V. CONCLUSIONS

The current study demonstrates that the tensile fracture of cast steel with porosity can be predicted from industrial radiographs using a porous metal plasticity material model commonly implemented in FEA software. Nine model material parameters were determined for sound WCB steel from its tensile curve. Using these model parameters and porosity fields mapped from the radiographs of the test specimens to nodes of FEA models, the tensile test curves for the castings with centerline porosity were simulated. Predicted and measured tensile curves compared well, and the measured and predicted elongation comparisons were also good. The most noticeable effect of porosity in cast steel is reduction in ductility, and the model predicted it well. It is difficult to make general statements about the effect of porosity on fracture behavior, since it has been demonstrated here that its effects are dependent on the porosity distribution relative to the load. For the seemingly small amounts of porosity shown here, where the average volumetric porosities in the gage sections of the specimens ranged from 0.10 to 0.27 pct, the ductility in the test castings with porosity is markedly reduced with the percent elongation data ranging from 12.8 to 19.6 pct *vs* 22 pct elongation for the sound material. This range of ductility behavior is due to the differing porosity distributions in the specimens. The current study demonstrates that the effect of porosity on ductility and fracture behaviors can be predicted provided that a reasonably accurate porosity field is used in the simulations.

Some disagreement still remains between prediction and measurement. The clearest factors contributing to the disagreement are ascribed to assumptions and limitations in the porous metal plasticity model, and the assumptions and deficiencies in determining how the porosity was distributed through the thickness of the plate specimens. The current study can be improved by more realistically reconstructing the porosity distribution through the plate thickness *via* tomography, for example. In addition to improving the fidelity of the measured porosity distributions, the authors plan to investigate whether porosity distributions predicted from casting simulation can be used in place of measured porosity distributions to accurately model the mechanical performance of castings.

ACKNOWLEDGMENTS

This research was undertaken through the American Metalcasting Consortium's (AMC) *Castings for Improved Readiness Research Program*. AMC is sponsored by Defense Supply Center Philadelphia (DSC, Philadelphia, PA) and the Defense Logistics Agency (DLA, Ft. Belvoir, VA). The current study was conducted under the auspices of the Steel Founders' Society of America (SFSA) through substantial in-kind support and guidance from SFSA member foundries. (Any opinions, findings, conclusions, or recommendations expressed herein are those of the authors and do not necessarily reflect the views of DSC, DLA, or the SFSA and any of its members.)

REFERENCES

1. T.L. Anderson: *Fracture Mechanics: Fundamentals and Applications*, Taylor & Francis, Boca Raton, FL, 2005, pp. 219–31.
2. R. Hardin and C. Beckermann: *Metall. Mater. Trans. A*, 2007, vol. 38A, pp. 2992–3006.
3. R.A. Hardin and C. Beckermann: *Metall. Mater. Trans. A*, 2009, vol. 40A, pp. 581–97.
4. P. Heuler, C. Berger, and J. Motz: *Fat. & Frac. of Eng. Mater. & Struc.*, 1992, vol. 16, pp. 115–36.
5. K.M. Sigl, R. Hardin, R.I. Stephens, and C. Beckermann: *Int. J. Cast Metals Res.*, 2004, vol. 17, pp. 130–46.
6. C.T. Herakovich and S.C. Baxter: *J. Mater. Sci.*, 1999, vol. 34, pp. 1595–1609.
7. A.P. Roberts and E.J. Garboczi: *J. Am. Ceram. Soc.*, 2000, vol. 83, pp. 3041–48.
8. N. Ramakrishnan and V.S. Arunachalam: *J. Am. Ceram. Soc.*, 1993, vol. 76, pp. 2745–52.
9. E. Zhang and B. Wang: *Int. J. Mech. Sci.*, 2005, vol. 47, pp. 744–56.
10. J.M. Dewey: *J. Appl. Phys.*, 1947, vol. 18, pp. 578–81.
11. A.L. Gurson: *J. Eng. Mater. Tech.*, 1977, vol. 99, pp. 2–15.
12. V. Tvergaard: *Int. J. Frac. Mech.*, 1981, vol. 17, pp. 389–407.

13. A. Needleman and V. Tvergaard: *J. Mech. Phys. Solids*, 1984, vol. 32, pp. 461–90.
14. ABAQUS Theory Manual, Version 6.10, section 4.3.6 Porous Metal Plasticity, Dassault Systèmes, Providence, RI, 2010, pp. 1–7.
15. N. Aravas: *Int. J. Num. Meth. Eng.*, 1987, vol. 24, pp. 1395–1416.
16. J. Besson: *Int. J. Damage Mech.*, 2010, vol. 19, pp. 3–52.
17. MAGMA GmbH, MAGMAsoft, Kackerstrasse 11, 52072 Aachen, Germany.
18. "Standard Test Methods for Tension Testing of Metallic Materials, Standard Designation: E8/E8M-11," ASTM International, West Conshohocken, PA, 2011, pp. 1–27.
19. "Standard Reference Radiographs for Steel Castings Up to 2 in. (51 mm) in Thickness, Standard Designation: E446," ASTM International, West Conshohocken, PA, 2011, pp. 1–4.
20. A.P. Roberts and E.J. Garboczi: *J. Am. Ceram. Soc.*, 2000, vol. 83, pp. 3041–48.